Earth and Planetary Science Letters 333–334 (2012) 122–133

Contents lists available at SciVerse ScienceDirect

Earth and Planetary Science Letters

journal homepage: www.elsevier.com/locate/epsl

Magnetotactic bacterial response to Antarctic dust supply during the Palaeocene–Eocene thermal maximum

Juan C. Larrasoaña [a,b,*], Andrew P. Roberts [b,c], Liao Chang [b,d], Stephen A. Schellenberg [e], John D. Fitz Gerald [b], Richard D. Norris [f], James C. Zachos [g]

[a] Instituto Geológico y Minero de España, Unidad de Zaragoza, C/Manuel Lasala 44, 9B, Zaragoza 50006, Spain
[b] Research School of Earth Sciences, The Australian National University, Canberra, ACT 0200, Australia
[c] School of Ocean and Earth Science, National Oceanography Centre, University of Southampton, European Way, Southampton SO14 3ZH, UK
[d] Palaeomagnetic Laboratory 'Fort Hoofddijk', Institute of Earth Sciences, Universiteit Utrecht, Budapestlaan 17, 3584 CD Utrecht, The Netherlands
[e] Department of Geological Sciences, San Diego State University, 5500 Campanile Drive, San Diego, CA 92182-1020, USA
[f] Scripps Institution of Oceanography, University of California, San Diego, 9500 Gilman Drive, La Jolla, CA 92093, USA
[g] Department of Earth and Planetary Sciences, University of California, Santa Cruz, CA 95064, USA

ARTICLE INFO

Article history:
Received 13 October 2011
Received in revised form
28 March 2012
Accepted 3 April 2012
Editor: P. DeMenocal

Keywords:
Palaeocene/Eocene thermal maximum
marine sediments
environmental magnetism
biogenic magnetite
aeolian dust

ABSTRACT

Distinct magnetic properties of marine sediments that record the Palaeocene–Eocene thermal maximum (PETM) have been suggested to be due to a bacterial magnetofossil signal that is linked to enhanced weathering conditions during the PETM. We document the dominance of bacterial magnetite in deep-sea sediments from southern Kerguelen Plateau (Ocean Drilling Program Hole 738C, southern Ocean) not only during the PETM, but also before and after the thermal event. This occurrence of magnetofossils throughout the PETM indicates that the occurrence of bacterial magnetosomes is not due to a preservation effect. Instead, we suggest that it is due to sustained mild iron-reducing conditions that dissolved the most labile aeolian-derived iron, which favoured continued magnetotactic bacterial activity without being strong enough to dissolve the less reactive magnetite and haematite. Enhanced aeolian haematite abundances at the beginning of the PETM indicate drier conditions on the neighbouring Antarctic continent at those times. Our results provide evidence that iron fertilisation by aeolian dust was the main limiting factor that conditioned proliferation of magnetotactic bacteria in the deep sea at the southern Kerguelen Plateau, with the exception of two short periods of rapidly changing palaeoenvironmental conditions at the onset and termination of the PETM. Increased iron supply from aeolian dust, that enhanced oceanic primary productivity and subsequent delivery of organic carbon to the seafloor, along with mild iron-reducing diagenetic conditions, seem to have been necessary to provide the iron needed for magnetite biomineralization by magnetotactic bacteria to drive their marked increase in abundance in the studied PETM record from southern Kerguelen Plateau. Our analyses of a deep-sea PETM record from Hole 1051B at Blake Nose (Atlantic Ocean) failed to identify magnetofossils despite evidence for the occurrence of magnetite and haematite of probable aeolian origin. Contrasting magnetic properties at these PETM sections indicate that further work is needed to understand the palaeoenvironmental and diagenetic factors whose interactions lead to production and preservation of magnetofossils in deep-sea sediments.

1. Introduction

Magnetotactic bacteria are prokaryotes that mineralise chains of membrane-enclosed crystals of magnetite or greigite that are known as magnetosomes (Bazylinski and Frankel, 2004; Faivre and Schüler, 2008; Kopp and Kirschvink, 2008). Magnetite-producing bacteria are often microaerophiles or nitrate reducers that thrive in the suboxic conditions found around the oxic–anoxic transition zone (OATZ), which, depending on the setting, can occur either within the water column, at the sediment/water interface, or within surface sediments (e.g. Kopp and Kirschvink, 2008). Magnetotactic bacteria use magnetosomes to align themselves with geomagnetic field lines, which facilitates their navigation within the specific chemical gradients in which they dwell. When magnetotactic bacteria die, magnetosomes accumulate and can be preserved as magnetofossils in the sediments. Due to the link between magnetotactic bacteria and specific redox conditions,

* Corresponding author at: Unidad de Zaragoza, Instituto Geológico y Minero de España, C/Manuel Lasala 44, 9B, 50006 Zaragoza, Spain. Tel.: +34 976555153; fax: +34 976 553358.
E-mail address: jc.larra@igme.es (J.C. Larrasoaña).

0012-821X/$ - see front matter © 2012 Elsevier B.V. All rights reserved.
http://dx.doi.org/10.1016/j.epsl.2012.04.003

magnetofossils have been proposed as recorders of environmental variations (Kopp and Kirschvink, 2008). Responses of magnetotactic bacteria to paleoenvironmental variations have been documented in association with Quaternary glacial–interglacial climate variability, which have been linked to changes in the supply of organic carbon and hence in seafloor redox conditions (Hesse, 1994; Tarduno and Wilkison, 1996; Lean and McCave, 1998; Yamazaki and Kawahata, 1998; Dinarès-Turell et al., 2003; Kopp and Kirschvink, 2008; Yamazaki, 2012).

Sustained oxic conditions typically result in suppression of magnetite biomineralization, and anoxic conditions drive dissolution of magnetofossils as sedimentation continues after bacterial death (Bazylinski and Frankel, 2004; Faivre and Schüler, 2008; Kopp and Kirschvink, 2008). These circumstances, along with undersampling of older sediments, have resulted in only rare reports of bacterial magnetite in pre-Quaternary marine sediments (see Kopp and Kirschvink, 2008). A notable exception is the Palaeocene–Eocene thermal maximum (PETM), which was a period of global warming at around 56 Ma that constitutes one of the most widely used analogues for global change (Dickens, 1999; Bains et al., 2000). Several authors have demonstrated the widespread occurrence of biogenic magnetite in PETM sediments from the mid-Atlantic US continental margin (Lippert and Zachos, 2007; Kopp et al., 2007, 2009; Schumann et al., 2008). Kopp et al. (2009) hypothesised that these magnetofossils preferentially accumulated near the mouth of an Amazon-like river, where increased sediment loads in response to warm and humid conditions delivered enhanced amounts of organic carbon and bioavailable iron to the continental shelf, thereby favouring proliferation of magnetotactic bacteria. The striking coincidence of magnetofossils with PETM sediments suggests, however, a preservation effect linked to establishment of a thick OATZ, which resulted from a transient increase in sedimentation rates that isolated PETM sediments from underlying sulphidic sediments (Dickens, 2008). Interpretation of magnetofossil abundances as proxies for magnetotactic bacterial activity is complicated, even when a preservation effect can be ruled out, if the OATZ is found within the sediments, because bacterial magnetite in this case would give rise to a post-depositional signal (Tarduno and Wilkison, 1996; Abrajevitch and Kodama, 2011).

Recent results from chalky deep-sea sediments from the southern Kerguelen Plateau (SKP) demonstrate the continued occurrence of magnetofossils throughout most of the Eocene, in connection with sustained suboxic conditions that favoured their formation and preservation (Roberts et al., 2011). These sediments therefore offer the rare opportunity to examine how magnetosomes can be used as palaeoenvironmental recorders. Here we present combined bulk magnetic, first-order reversal curve (FORC), ferromagnetic resonance (FMR) and transmission electron microscope (TEM) analyses of PETM sediments from Ocean Drilling Program (ODP) Hole 738C from the SKP. Our results are used to decipher the response of otherwise poorly preserved magnetotactic bacterial populations to climate variability during an analogue for present-day global warming. This is important because bacteria account for a large fraction of the total biomass and might play an important role in the carbon cycle (Stanley, 2010). Furthermore, the presence of bacterial magnetite in these pelagic carbonate sediments is important for preservation of palaeomagnetic signals in such environments.

2. Materials and methods

Hole 738C was cored on the SKP (Fig. 1), which was close to the Antarctic margin during the PETM, at a water depth of 2253 m. The PETM section at this hole comprises a white calcareous foraminiferal nannofossil chalk with some evidence of bioturbation. These sediments accumulated at a water depth of 2000–2500 m (Shipboard Scientific Party, 1989) at a palaeolatitude of about 61°S (see Besse and Courtillot, 2002; Ali and Aitchison, 2009) (Fig. 1). The clay mineral composition of the non-carbonate fraction, which is characterised by a mixture of smectite, illite, chlorite and kaolinite, indicates humid conditions on the Antarctic margin in the late Palaeocene and early Eocene despite its high latitude position (Ehrmann, 1991; Ehrmann and Mackensen, 1992).

Sediment chips ($\leq 0.5 \times 0.5 \times 0.5$ cm^3) were taken with a mean stratigraphic resolution of 4 cm, which was reduced to 1 cm at the onset and termination of the CIE and widened to 10 cm in the rest of the studied interval. Magnetic measurements were carried out at the National Oceanography Centre, Southampton (NOCS) and include: (1) low-field magnetic susceptibility (χ), which was measured using a MS2B Bartington Instruments magnetic susceptibility bridge with a field of 0.1 mT at a frequency of 470 Hz; (2) anhysteretic remanent magnetisation (ARM), which was applied with a 2-G Enterprises in-line alternating field (AF) demagnetizer using a DC bias field of 0.05 mT parallel to an axially-oriented peak AF of 100 mT while the sample was passed through the

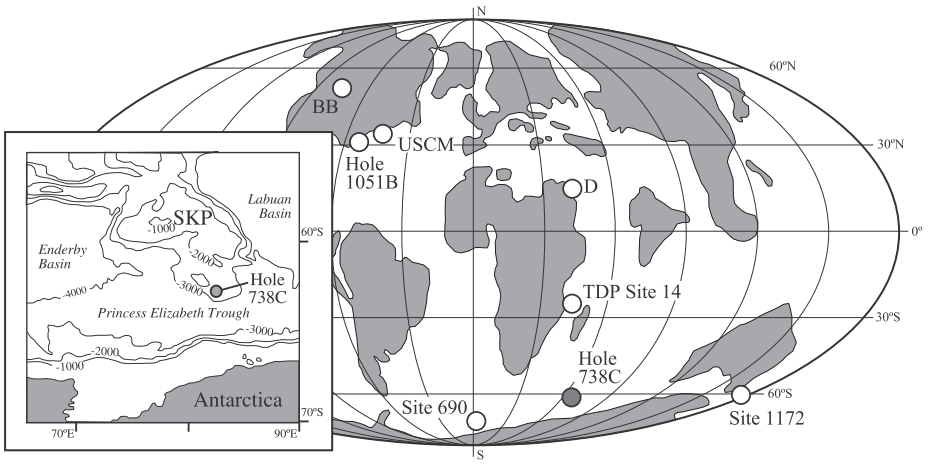

Fig. 1. Paleogeographic reconstruction of emerged land at the PETM (after Schulte et al., 2011), with location of ODP Hole 738C and of other sites mentioned in the text. USCM: US mid-continental margin; D: Dababiya section; BB: Bighorn Basin. The inset is a detailed map that includes the location of ODP Hole 738C on southern Kerguelen Plateau (SKP) in its present-day configuration.

demagnetizer at 8 cm/s; and (3) a set of two isothermal remanent magnetisations applied at a field of 1 T ($IRM_{1\ T}$) and at a back-field of 0.3 T ($IRM_{-0.3\ T}$) using a pulse magnetiser. ARMs and IRMs were measured using a 2-G Enterprises three-axis cryogenic magnetometer at NOCS. All magnetic properties are normalised by mass. We also calculated a suite of conventional magnetic parameters that include the ratio between the ARM susceptibility and the bulk magnetic susceptibility (χ_{ARM}/χ; Banerjee et al., 1981; King et al., 1982), the S-ratio ($=0.5\times[1-(IRM_{-0.3\ T}/IRM_{1\ T}]$); Bloemendal et al., 1992), and the HIRM ($=0.5\times(IRM_{1\ T}-IRM_{-0.3\ T})$; Bloemendal et al., 1992). ARM and χ_{ARM}/χ have been used as proxies for the concentration and grain size of magnetite, respectively (Banerjee et al., 1981; King et al., 1982; Evans and Heller, 2003; Peters and Dekkers, 2003). The S-ratio and HIRM have been used to make inferences about relative variations between high- and low-coercivity minerals and the concentration of high-coercivity minerals, respectively (Bloemendal et al., 1992). Sub-sampling enabled additional measurement of magnetic hysteresis parameters and FORC diagrams for discriminating magnetic mineralogy, domain state, and magnetic interactions among magnetic particles (Day et al., 1977; Roberts et al., 2000). Egli et al. (2010) demonstrated that intact magnetosome chains have a characteristic magnetic signature associated with uniaxial non-interacting single domain (SD) particles that can be clearly identified using FORC diagrams. We used the FORC measurement parameters specified by Egli et al. (2010) to detect such particles. FORC measurements were made on ~700–800 mg samples using a Princeton Measurements Corporation vibrating sample magnetometer. Averaging times varied between 150 and 500 ms depending on the magnetisation of the sample; results were less noisy for longer averaging times. FORC diagrams were produced using the software of Egli et al. (2010) with a smoothing factor of 5 (Roberts et al., 2000).

FMR spectroscopy can probe unpaired electrons within samples, and has therefore become a standard technique for studying magnetic particle systems. FMR has been developed recently to detect the magnetic anisotropy associated with magnetosome chain structures within bulk sediment samples (Weiss et al., 2004; Kopp et al., 2006, 2007; Fischer et al., 2008; Charilaou et al., 2011; Gehring et al., 2011; Roberts et al., 2011). We have therefore made FMR measurements on bulk carbonate sediments from ODP Hole 738C to test for the presence of magnetite magnetofossils. FMR spectra were measured using an X-band Bruker EMX microspectrometer at the School of Chemistry, University of Manchester, UK. For each measurement, 100–200 mg of air-dried sediment was loaded into FMR glass tubes and microwaved at a frequency of ~9.4 GHz and power of ~632 μW. All spectra were integrated over three magnetic field sweeps from 0 to 700 mT.

Extraction of magnetic particles for TEM analysis was performed for samples from ODP Hole 738C following an adaption of the procedures of Stolz et al. (1986) and Hesse (1994). Magnetic extracts were viewed and analysed using a Philips CM300 TEM operated at 300 kV in the Research School of Earth Sciences, Australian National University. This instrument is equipped with an EDAX Phoenix retractable X-ray detector (with ultra-thin window) and a Gatan 694 slow-scan digital camera.

A high-resolution bulk carbonate stable isotope record was generated for Hole 738C with samples collected every 1 cm. Analyses were carried out on a PRISM III gas source mass spectrometer coupled to an Autocarb acid reaction system in which samples are dissolved in phosphoric acid at 90 °C, and the CO_2 distilled in a single step. Carbonate sediment contents (wt%) were measured using 5–10 mg of dry bulk sediment powder on a UIC coulometer for samples taken in the same stratigraphic horizons where chips for rock magnetic analyses were collected.

3. Results

Carbon isotope data indicate that the carbon isotope excursion (CIE) associated with the PETM spans ~110 cm and involves a −2.5‰ shift in $\delta^{13}C$ values (Fig. 2a) (Supplementary data, Table 1). The CIE begins at ~285.5 mbsf with a rapid $\delta^{13}C$ shift to lighter values (event c in Fig. 2a). This shift is followed by a transient relative stabilisation (d) and a second rapid shift toward lighter values (e). The lowest $\delta^{13}C$ values are found at a final $\delta^{13}C$ shift at ~285.2 mbsf (g) that follows a prolonged relative stabilisation event (f). After the main part of the CIE, $\delta^{13}C$ values increase rapidly (event h), with an inflection (i), and gradually level off so that the excursion terminates at ca 284.4 mbsf (Fig. 2a).

Carbonate data indicate a rapid shift from high (around 90 wt%) carbonate contents before the CIE to lowest (ca. 70 wt%) contents at its onset (Fig. 2b). Carbonate contents rapidly recover so that they are similar (around 90 wt%) to pre-PETM values before reaching the main part of the CIE (event g) and above. This pattern attests to dissolution of carbonates in the lower part of the CIE in response to periods of rapid ocean acidification during the beginning of the PETM (Zachos et al., 2005).

The S-ratio varies between 0.97 and 1 through the PETM interval of Hole 738C (Fig. 2c), which is consistent with the dominance of magnetite (Bloemendal et al., 1992; Frank and Nowaczyk, 2008). Given the dominance of magnetite and, hence, the similarity between $IRM_{1\ T}$ and $IRM_{-0.3\ T}$, some S-ratios give unrealistic values slightly exceeding 1; these values have been set to 1. ARM values indicate (Fig. 2d) that magnetite concentration is relatively constant before, after and throughout much of the CIE, but with strikingly high abundance peaks that coincide with major $\delta^{13}C$ shifts at the beginning of the CIE (e.g., events c, e). Intervals characterised by increased magnetite concentrations coincide with shifts to both lighter (event c) and heavier (event h) $\delta^{13}C$ values, whereas intervals characterised by decreasing magnetite concentrations typically coincide with lighter $\delta^{13}C$ values (events e, g). During periods with stable $\delta^{13}C$ values (events d, f), the magnetite concentration stabilizes. χ_{ARM}/χ values range between 5 and 25 (Fig. 2e) and are consistent with the presence of SD magnetite (Peters and Dekkers, 2003). The most conspicuous χ_{ARM}/χ variations involve a shift to relatively coarser magnetite grains at the onset of the CIE (event d) and the shift to relatively finer grains at around event h. HIRM oscillates around $0–1\times10^{-6}$ Am^2/kg before, after and throughout much of the CIE, and has highest values of up to 1×10^{-6} Am^2/kg at the beginning of the $\delta^{13}C$ excursion (small, unrealistic negative HIRM values that result from the similarity between $IRM_{1\ T}$ and $IRM_{-0.3\ T}$ have been set to 0) (Fig. 2g). Rock magnetic data indicate that the high-coercivity mineral responsible for variations in HIRM at the studied site is haematite (Roberts et al., 2011).

Values of hysteresis ratios lie close to the SD field of Day et al. (1977), following a girdle along the theoretical line that represents a mixture of about 60–90% of equidimensional SD magnetite with 30–10% of multi-domain (MD) magnetite (Dunlop, 2002) (Fig. 3, Table 1). The mean M_r/M_s value is 0.39, which is close to the theoretical value of 0.5 for uniaxial SD magnetite grains and similar to other PETM sediments where SD magnetite of biogenic origin has been reported within the CIE (Kent et al., 2003; Lippert and Zachos, 2007; Kopp et al., 2007). At Hole 738C, M_r/M_s ranges between 0.36 and 0.43 before, during, and after most of the CIE, and drops to 0.32 at its onset (Fig. 2f and Fig. 3, Table 1).

FORC distributions are nearly identical for all samples studied (Fig. 4a–h), with a sharply peaked vertical distribution (Fig. 4i), and are characterised by coercivity distributions that peak between 17 and 30 mT (Fig. 4j). These distributions indicate the

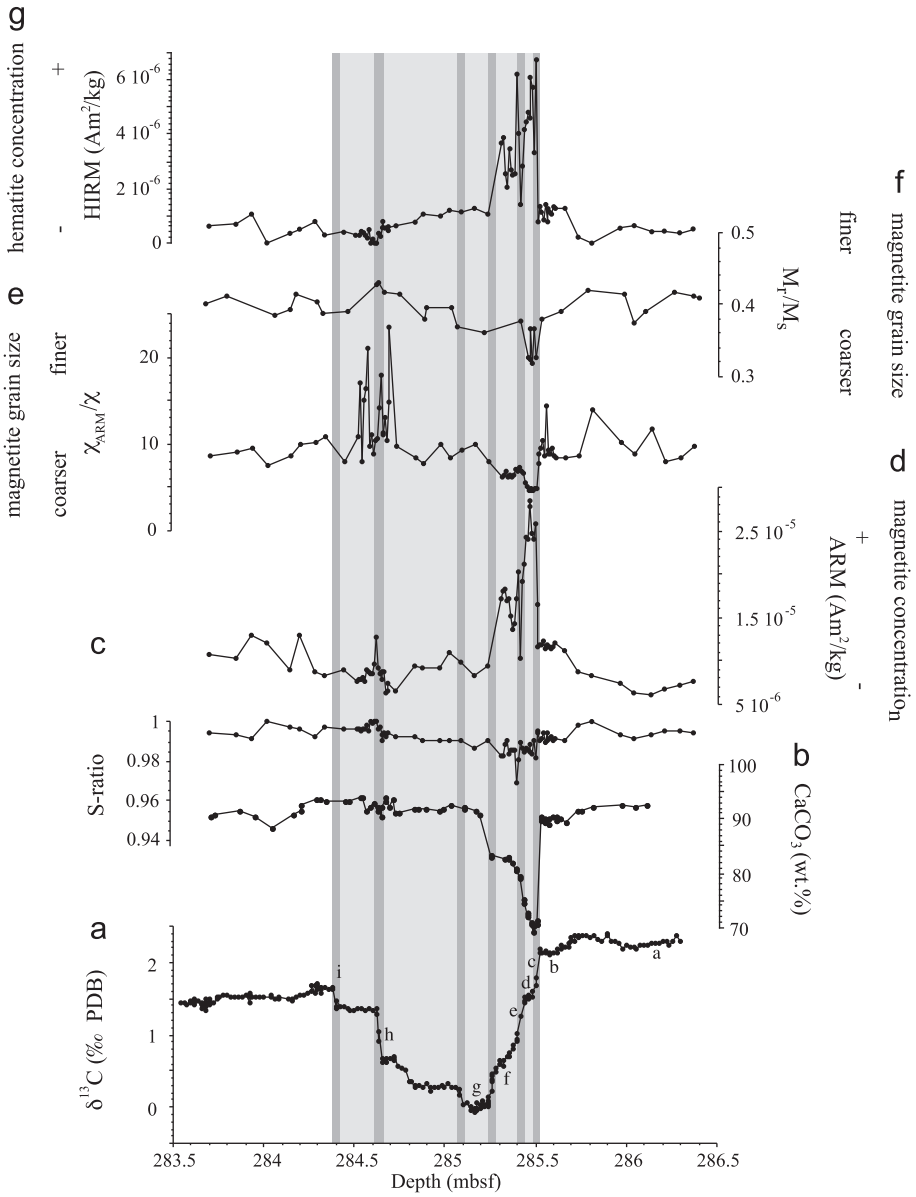

Fig. 2. Down-core variations in (a) bulk-sediment carbon isotopes, (b) carbonate contents, and (c) mineralogy-, (d, g) magnetic mineral concentration-, and (e, f) grain size-dependent magnetic properties across the PETM at ODP Hole 738C.

predominance of non-interacting magnetite particles within a narrow SD grain-size range (Roberts et al., 2000; Egli et al., 2010), not only during but also before and after the CIE. The less well-defined outer parts of the FORC diagrams indicate a secondary contribution from a coarser-grained pseudo-single domain (PSD) and MD particle assemblage (Roberts et al., 2000). The dominant non-interacting SD ridge on the FORC distributions (Fig. 4) is characteristic of intact magnetosome chains (Egli et al., 2010). A non-interacting SD magnetic particle assemblage will produce a ridge with a finite width rather than an ideal delta-function spike because of the discrete nature of the FORC measurement steps and because of smoothing (Egli et al., 2010). Nevertheless, the sharp ridge that is fitted with a Lorentzian function through the smoothed (SF=5) data (Fig. 4i) is consistent with a lack of negative (e.g., between magnetofossil chains) magnetostatic interactions in the magnetic particle assemblage. Profiles along the peak of the coercivity distribution have maxima at 17–30 mT, and are best fitted by a skewed Gaussian distribution (Fig. 4j) rather than by a normal or log-normal distribution. A negatively skewed Gaussian grain-size distribution is typical of magnetite magnetosomes produced by uncultured magnetotactic bacteria, where the distribution is truncated at the maximum size for stable SD grains (Arató et al., 2005; Kopp and Kirschvink, 2008). The positively skewed Gaussian profiles shown in Fig. 4j are consistent with this expectation when considering the coercivity distribution that will be produced by typical variations in magnetosome width/length ratio (e.g., Arató et al., 2005) in addition to the negatively skewed Gaussian grain-size distribution. Kopp and Kirschvink (2008) described a similar range of coercivities for magnetite magnetosomes as those shown in Fig. 4j.

All measured FMR spectra contain sharp lines (6 intense lines and 10 weak lines, Fig. 5a) that represent the FMR signal for Mn^{2+} (Boughriet et al., 1992; Otamendi et al., 2006), which is a common cation in calcite. In addition to the strong Mn^{2+} signal linked to calcite, the broad spectra are associated with magnetically ordered minerals. In order to remove the strong Mn^{2+} sextet signals and to analyse the broad FMR signals (Fig. 5a), we used Fast Fourier Transform (FFT) smoothing to process the measured FMR spectra. This smoothing procedure effectively removes the large Mn^{2+} signal and noisy data, and leaves the broad FMR

Table 1
Magnetic hysteresis parameters for samples from Hole 738C.

Hole	Section	Interval (cm)	Depth (mbsf)	M_r/M_s	B_{cr}/B_c
738C	11R1	28.0	283.68	0.402	1.658
738C	11R1	40.0	283.80	0.412	1.715
738C	11R1	66.0	284.06	0.384	1.672
738C	11R1	75.0	284.15	0.393	1.626
738C	11R1	78.0	284.18	0.415	1.661
738C	11R1	89.0	284.29	0.405	1.581
738C	11R1	92.0	284.32	0.387	1.669
738C	11R1	106.0	284.46	0.390	1.618
738C	11R1	122.5	284.62	0.428	1.603
738C	11R1	123.0	284.63	0.430	1.640
738C	11R1	126.0	284.66	0.417	1.589
738C	11R1	135.0	284.75	0.415	1.580
738C	11R1	148.0	284.88	0.380	1.599
738C	11R1	149.0	284.89	0.395	1.634
738C	11R2	13.0	285.03	0.396	1.599
738C	11R2	16.0	285.06	0.369	1.621
738C	11R2	31.0	285.21	0.362	1.700
738C	11R2	51.0	285.41	0.378	1.619
738C	11R2	55.5	285.45	0.325	1.809
738C	11R2	56.5	285.46	0.324	1.819
738C	11R2	57.0	285.47	0.366	1.686
738C	11R2	57.5	285.48	0.317	1.815
738C	11R2	59.0	285.49	0.365	1.660
738C	11R2	60.0	285.50	0.325	1.786
738C	11R2	63.0	285.53	0.379	1.637
738C	11R2	73.0	285.63	0.391	1.645
738C	11R2	88.0	285.78	0.421	1.591
738C	11R2	107.5	285.98	0.415	1.553
738C	11R2	114.0	286.04	0.373	1.604
738C	11R2	120.0	286.10	0.390	1.613
738C	11R2	136.0	286.26	0.418	1.611
738C	11R2	146.0	286.36	0.412	1.546
738C	11R2	149.0	286.39	0.408	1.573

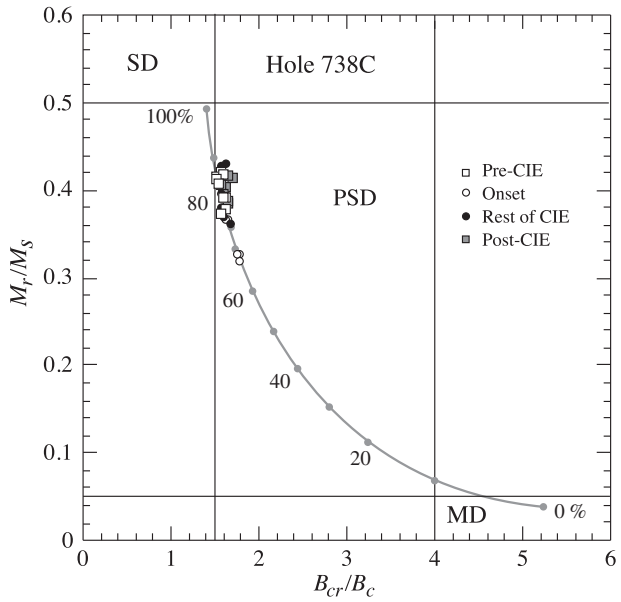

Fig. 3. Magnetic hysteresis results from Hole 738C plotted in a Day diagram (cf. Day et al., 1977). The line represents the theoretical mixing curve of MD and variable percentages (grey points) of cubic SD magnetite (Dunlop, 2002). SD=single domain, PSD=pseudo-single domain, and MD=multi-domain data fields from Day et al. (1977).

signal unaffected (Fig. 5b). The measured FMR spectra have two clearly evident maxima at low applied fields and are asymmetrically extended to the low field direction. These shapes of FMR spectra are uniquely distinctive of intact magnetite magnetosome chains (Weiss et al., 2004; Kopp et al., 2006; Fischer et al., 2008; Charilaou et al., 2011; Gehring et al., 2011). After FFT analysis, the smoothed derivative FMR spectra (red line in Fig. 5b) were integrated (Fig. 5c). We use the same FMR parameters, defined in the integrated spectra (Fig. 5c), as those proposed by Weiss et al. (2004) and Kopp et al. (2006) to describe the spectra (Fig. 5c; Table 2). B_{eff} is the maximum absorption field in the integrated spectra (Fig. 5c), which is also the field at the zero crossing point in the derivative spectra (Fig. 5b). The effective spectroscopic g-factor, g_{eff}, associated with maximum absorption is given by

$$g_{eff} = h\nu/\mu_B B_{eff},$$

where h ($=6.626\times10^{-34}$ Js) is Planck's constant, ν is the microwave frequency, and μ_B ($=9.274\times10^{-24}$ J/T) is the Bohr magnetron. B_{low} and B_{high} indicate the fields where the absorptions are half values of maximum absorption in the integrated spectra (Fig. 5c). ΔB_{low} and ΔB_{high} are the distances between B_{eff} and B_{low}, and between B_{high} and B_{eff}, respectively (Fig. 5c). The line width ΔB_{FWHM} is the sum of ΔB_{low} and ΔB_{high}. The asymmetry ratio A is the ratio of ΔB_{high} and ΔB_{low}.

Values of g_{eff} are consistently 1.97–2.05 (Table 2), which falls within the range $g_{eff}<2.12$ for almost all published samples that contain magnetite magnetosomes. A is also much lower than 1 (Table 2), which suggests that the spectra shift toward lower fields. Kopp et al. (2006) found their α parameter, which is defined as a range of linear contours in ΔB versus A diagrams, useful for distinguishing between biogenic ($\alpha<0.25$) and abiogenic ($\alpha>0.40$) magnetite. For the studied samples, $\alpha=0.24-0.28$ (Table 2), which fall within the range of values for sedimentary samples with significant biogenic magnetite concentrations (Kopp et al., 2006, 2007, 2009). The shape of the FMR spectra, and the values of parameters derived from these spectra, are all characteristic of FMR spectra for intact magnetite magnetosome chains (Weiss et al., 2004; Kopp et al., 2006, 2007; Fischer et al., 2008; Charilaou et al., 2011; Gehring et al., 2011; Roberts et al., 2011).

TEM observations of magnetic separates for sediments from ODP Hole 738C indicate the presence of abundant small iron oxide particles with regular morphology (Fig. 6a–c). High-resolution TEM images (Fig. 6d), selected area electron diffraction patterns (Fig. 6e, f), and energy dispersive x-ray spectroscopic (EDS) analysis (Fig. 6g) consistently indicate that these particles consist of magnetite. The length of the nanoparticles ranges between ~30 and ~220 nm, with most magnetosomes having lengths between ~40 and ~150 nm (Fig. 7). These lengths, along with axial ratios ranging between 1 and 0.15, indicate that most magnetosomes fall within the theoretically expected range for equidimensional and elongated SD magnetite (Butler and Banerjee, 1975; Muxworthy and Williams, 2006; Kopp and Kirschvink, 2008). Magnetosomes have various well-defined crystal morphologies, including octahedra, cubo-octahedra, and hexagonal prisms, which are typical of magnetosome crystals found in living magnetotactic bacteria (Kopp and Kirschvink, 2008). Short chains of magnetite crystals are also commonly observed (Fig. 6b) despite disaggregation of the sediment during the extraction procedure. These observations confirm indications from FORC and FMR measurements that the magnetic properties of the studied PETM sediments from Hole 738C are dominated by abundant intact magnetofossil chains that are preserved within the sediments. In this regard, PETM sediments from Hole 738C provide a maximum score in the scheme developed by Kopp and Kirschvink (2008) for robust identification of magnetofossils in the sedimentary record.

4. Discussion

Magnetic parameters that are used as proxies for the concentration of magnetite (ARM) and haematite (HIRM) have been

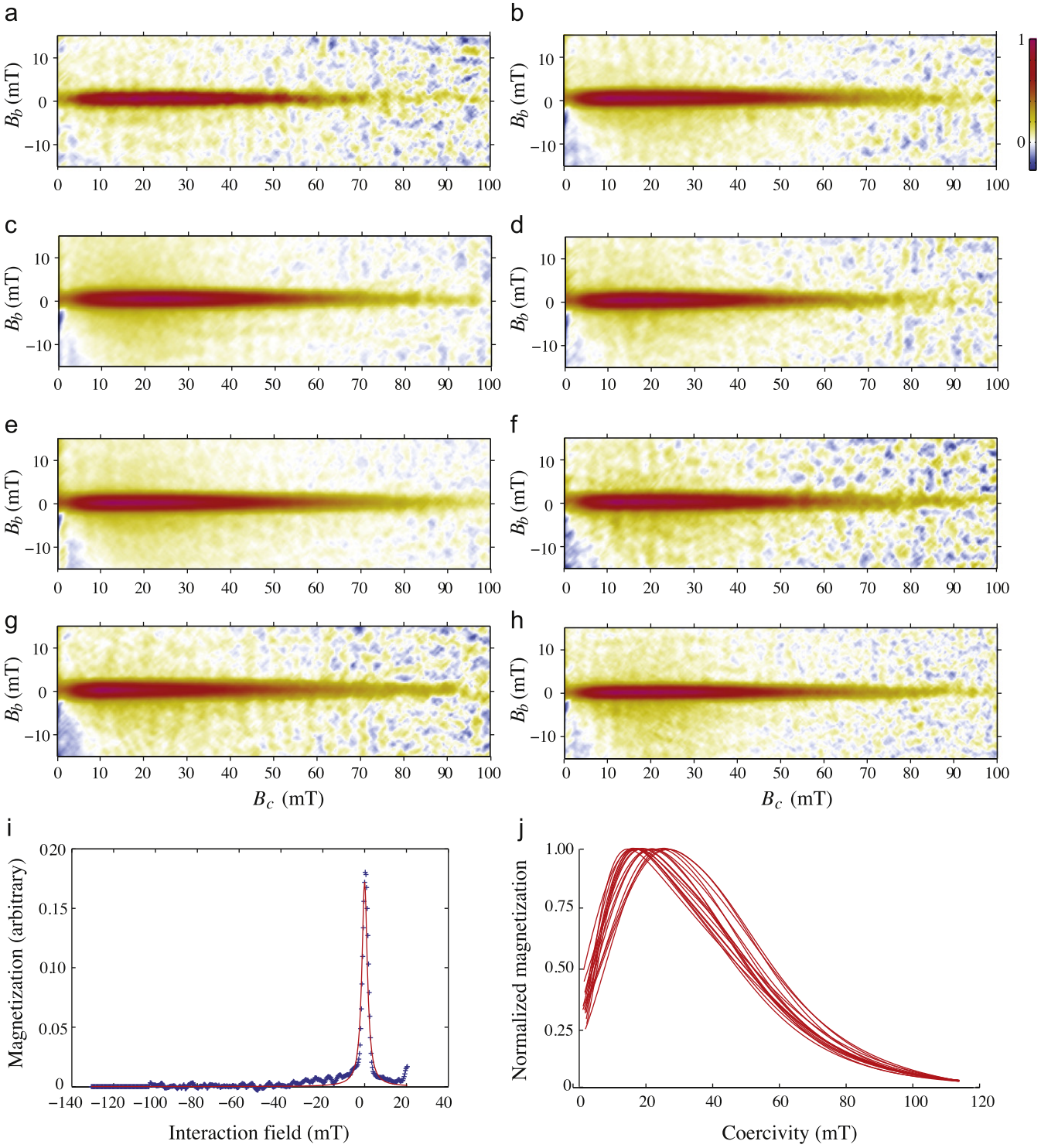

Fig. 4. Representative FORC diagrams for samples (a, b) before, (c) at the onset, (d–f) during, and (g, h) after the PETM CIE in ODP Hole 738C. All of the FORC diagrams are similar and indicate the presence of magnetostatically non-interacting SD magnetic particle assemblages that are typical of intact magnetite magnetofossil chains (cf. Egli et al., 2010). FORC signatures associated with intact magnetofossil chains are also illustrated in (i) and (j), where: (i) a vertical profile through the peak of the FORC distribution has a sharp ridge that is best fit by a Lorentzian distribution (i.e. a distribution of horizontal distances at which a tilted line segment cuts the *x* axis), and (j) horizontal profiles through the peak of 17 FORC distributions, which indicate coercivities that are best fitted with skewed Gaussian distributions with peaks ranging between 17 and 30 mT (see text for discussion). In all cases, the smoothing factor for the FORC diagrams (Roberts et al., 2000) is 5.

calculated on a carbonate-free basis (CFB) in order to account for dilution by carbonate (ARM–CFB and HIRM–CFB hereafter) (Fig. 8). HIRM–CFB has values that range between 0 and 1×10^{-5} Am^2/kg before the CIE and experience a rapid shift up to 2.2×10^{-5} Am^2/kg at the onset of the CIE (event c) (Fig. 8b). HIRM–CFB values remain high up to event f, and then progressively decline to background values of between 0 and 1×10^{-5} Am^2/kg event h. In contrast to HIRM, ARM–CFB values have a strikingly different pattern of variability across the PETM compared to those not corrected for carbonate contents (Fig. 8c).

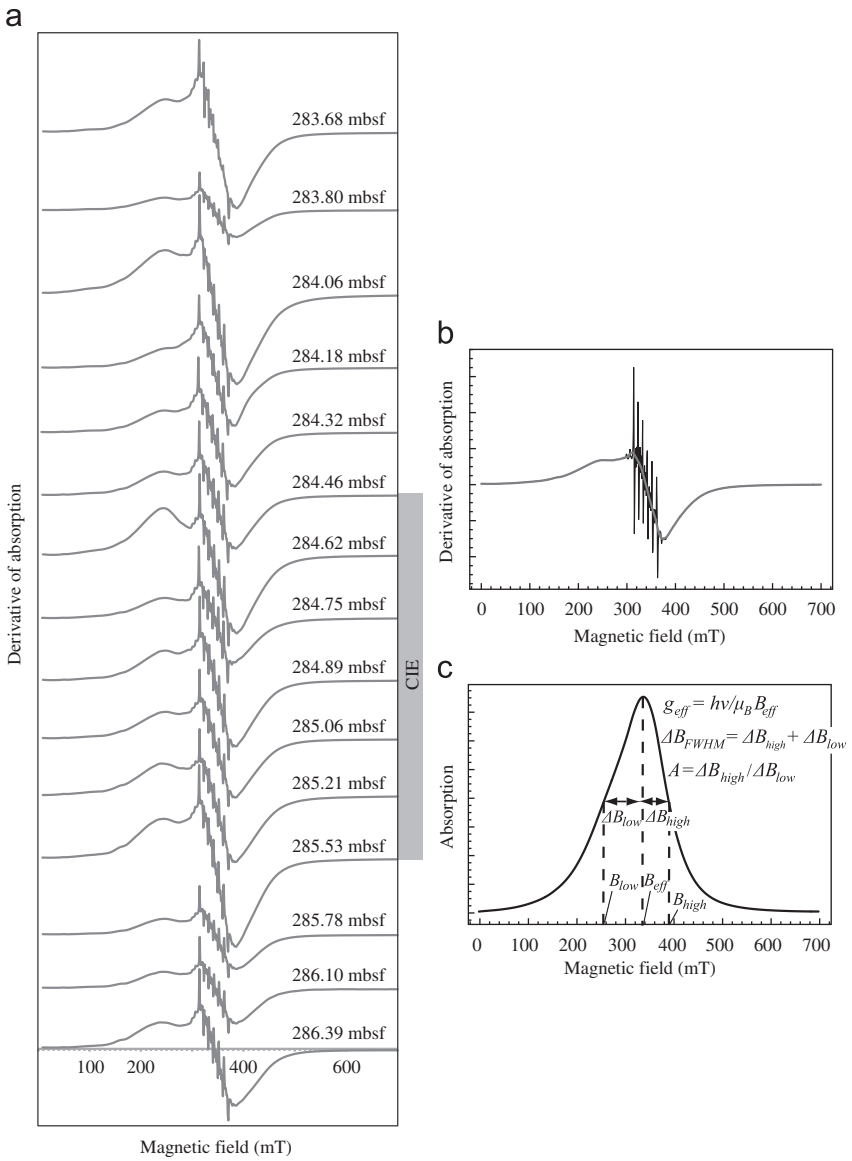

Fig. 5. FMR spectra from ODP Hole 738C. (a) Spectra for bulk carbonate samples from ODP Hole 738C (depths of samples are indicated on each spectrum) derived after averaging the original experimental data. Each spectrum has been normalised by sample mass so that the respective spectra can be compared directly as shown. (b) An example illustrating the use of FFT smoothing to remove the sharp Mn^{2+} FMR sextet signals and noise. Raw data are shown in black, while the FFT smoothed representation is shown in grey. (c) Integration of the FFT smoothed FMR spectrum (red curve) in (b). Characteristic parameters used for analysing FMR spectra for typical results from ODP Hole 738C are defined in the integrated spectra, following Weiss et al. (2004) and Kopp et al. (2006).

The onset of the CIE is characterised by a rapid shift to lower ARM–CFB values (Fig. 8c) instead of markedly increasing (Fig. 2e). Throughout the rest of the record, ARM–CFB values undergo minor variations around a mean value of 1×10^{-4} Am^2/kg. Regardless, with the exception of the interval through events c–e and around event h, the ARM–CFB signal varies in phase with HIRM–CFB values (see arrows in Fig. 8).

No evidence of ice rafting has been reported for the SKP up to 45.5 Ma (Lutetian, Middle Eocene) (Ehrmann and Mackensen, 1992). The lack of turbidites around the PETM at Hole 738C (Ehrmann, 1991) and the presence of the deep-water Princess Elizabeth Trough (Fig. 1), which has existed near its present-day configuration since the Late Cretaceous (Ali and Aitchison, 2009) and separates the SKP from Antarctica, also excludes an Antarctic riverine (either as bed load or suspended load) source for haematite. Riverine supply from the SKP can be also rejected as a potential source of haematite because it has been submerged since at least 85 Ma (Late Cretaceous) (Frey et al., 2000; Ali and Aitchison, 2009). Terrigenous material in the Hole 738C PETM sediments is clay-sized (Ehrmann and Mackensen, 1992); the clay minerals and haematite are most likely to represent an aeolian dust component derived from Antarctica. Aeolian dust has been also argued to be the main terrigenous component of Eocene sediments from Hole 738C (Roberts et al., 2011) and from Early Paleogene sediments at much more distal positions within the central Pacific Ocean (Woodard et al., 2011). The most likely explanation for aeolian haematite contents peaking in the lower half of the CIE (Fig. 8; events c–f) is an increase in aridity on the neighbouring Antarctic continent in response to rising global temperatures during the PETM. Subsequently, aeolian haematite contents decreased progressively to the same background values that preceded the CIE, which indicates a progressive shift back to the climatic conditions that prevailed before the PETM. A similar situation has been described from the Dababiya PETM section in

Table 2
FMR parameters for samples from Hole 738C.

Hole	Section	Interval (cm)	Depth (mbsf)	B_{eff} (mT)	g_{eff}	B_{low} (mT)	B_{high} (mT)	ΔB_{low} (mT)	ΔB_{high} (mT)	A	ΔB_{FWHM} (mT)	α
738C	11R1	28.0	283.68	338.5	1.98	261.6	393.9	76.9	55.4	0.72	132.3	0.25
738C	11R1	40.0	283.80	337.5	1.99	255.8	393.6	81.7	56.1	0.69	137.8	0.25
738C	11R1	66.0	284.06	334.8	2.01	243.8	397.0	91.0	62.2	0.68	153.2	0.27
738C	11R1	78.0	284.18	338.5	1.98	274.3	387.5	64.3	48.9	0.76	113.2	0.24
738C	11R1	92.0	284.32	339.2	1.98	264.7	391.9	74.6	52.7	0.71	127.2	0.24
738C	11R1	106.0	284.46	337.9	1.99	255.5	392.9	82.4	55.1	0.67	137.5	0.25
738C	11R1	122.5	284.62	333.8	2.01	238.7	395.0	95.1	61.2	0.64	156.3	0.26
738C	11R1	135.0	284.75	341.3	1.97	257.5	395.0	83.8	53.7	0.64	137.5	0.24
738C	11R1	149.0	284.89	339.6	1.98	257.5	393.6	82.1	54.0	0.66	136.1	0.25
738C	11R2	16.0	285.06	338.5	1.98	253.7	395.0	84.8	56.4	0.67	141.2	0.25
738C	11R2	31.0	285.21	336.8	1.99	242.8	396.3	94.0	59.5	0.63	153.6	0.26
738C	11R2	51.5	285.41	338.5	1.98	255.1	392.2	83.4	53.7	0.64	137.1	0.24
738C	11R2	63.0	285.53	338.9	1.98	252.4	395.7	86.5	56.8	0.66	143.3	0.25
738C	11R2	73.0	285.63	339.9	1.98	240.4	402.5	99.5	62.6	0.63	162.1	0.27
738C	11R2	88.0	285.78	341.3	1.97	255.5	396.0	85.8	54.7	0.64	140.5	0.25
738C	11R2	107.5	285.98	328.3	2.05	239.0	395.7	89.3	67.4	0.75	156.6	0.28
738C	11R2	120.0	286.10	340.3	1.97	253.1	397.0	87.2	56.8	0.65	144.0	0.25
738C	11R2	136.0	286.26	338.9	1.98	245.9	398.7	93.0	59.8	0.64	152.9	0.26
738C	11R2	149.0	286.39	339.2	1.98	249.6	398.1	89.6	58.8	0.66	148.4	0.26

North Africa (Schulte et al., 2011), where an increase in aeolian dust supply with respect to riverine input was reported in connection with drier, likely more seasonal, climatic conditions. Drier conditions at the beginning of the CIE have also been reported from the Bighorn Basin in North America (Wing et al., 2005; Kraus and Riggins, 2007; Smith et al., 2009) and from Tanzania Drilling Project Site 14 in subtropical East Africa (Handley et al., 2012). Decreased river discharge into the East Tasman Plateau, resulting from the interaction between climate and sea-level, has also been proposed during the PETM from ODP Site 1172 (Sluijs et al., 2011). Our data therefore support the emerging idea that the interior of continents experienced drier conditions, at least seasonally, at the beginning of the CIE despite a globally enhanced hydrological cycle during the PETM (Bowen et al., 2004; Schmitz and Pujalte, 2007). The clay mineral assemblage of sediments from ODP Site 690 indicates enhanced weathering regimes, and hence seasonally wetter conditions, in East Antarctica, mainly late in the PETM (Kelly et al., 2005), which is consistent with our inference of drier (at least seasonally) conditions in West Antarctica at the onset of the thermal event. Enhanced deflation of silt-sized particles as aeolian dust is often associated with dry events that follow humid periods during which fluvial transportation provided increased amounts of deflatable silt (e.g. Maher et al., 2010). Overall, our results suggest that the response of the hydrological cycle to global warming during the PETM was variable even at a regional or seasonal scale.

Bulk magnetic, hysteresis, FORC, FMR and TEM analyses of Hole 738C sediments demonstrate that biogenic magnetite is the dominant magnetic mineral not only during the PETM as has been previously reported in other sections (Lippert and Zachos, 2007; Kopp et al., 2007, 2009; Schumann et al., 2008), but also before and after the thermal event. Widespread accumulation of magnetosomes before the PETM provides additional evidence that the association of SD magnetite with the PETM cannot be related to a comet impact (see Kent et al., 2003; Cramer and Kent, 2005). On the other hand, the dominance of fossil magnetosomes before, during and after the CIE makes the Hole 738C record the only PETM section reported where a preservation effect can be convincingly excluded for explaining the occurrence of bacterial magnetosomes. With the exception of the intervals through events c–e and around event h, magnetosome concentrations mimic haematite abundances (Fig. 8) thereby indicating a reliable production signal for magnetosome abundances. For magnetosomes to carry such a pristine palaeoenvironmental signal, which is not significantly lagged with respect to changes in haematite abundances, the OATZ must have been established around or above the sediment/water interface.

Roberts et al. (2011) recently provided evidence for the importance of availability of dissolved iron, supplied by aeolian dust, as a major limiting factor for magnetotactic bacterial abundances in Eocene sediments from the adjacent ODP Hole 738B. They argued that enhanced fluxes of aeolian dust would have provided iron, which is a limiting micronutrient, to oligotrophic surface waters that would have increased primary productivity. Increased export of organic carbon to the seafloor is widely observed in association with natural iron fertilisation (Blain et al., 2007; Pollard et al., 2007). This would have fuelled magnetotactic bacterial metabolism by providing a source of metabolisable organic carbon that would have also promoted suboxic iron-reducing conditions. Under suboxic conditions, the most labile iron-bearing minerals, such as hydrous ferric oxide and lepidocrocite (Poulton et al., 2004), would have dissolved to provide the source of iron required for magnetosome biomineralization (Roberts et al., 2011). Preservation of magnetite and haematite throughout the studied interval of Hole 738C indicates that iron-reducing conditions were mild and that these less reactive minerals did not undergo dissolution either before, during, or after the CIE. Such conditions evidently extended throughout the Eocene and across the Cretaceous–Tertiary boundary, respectively, at Site 738 as demonstrated by Roberts et al. (2011) and Abrajevitch and Kodama (2009).

Coincidence between magnetosome concentrations and haematite abundances throughout most of the CIE (Fig. 8) suggests an immediate response of magnetotactic bacterial activity to enhanced aeolian dust fluxes and hence to availability of dissolved iron. However, the striking decoupling between magnetosome abundances and aeolian dust fluxes observed at the onset of the CIE (events c–e) and around event h, which are associated with the fastest $\delta^{13}C$ shifts (Fig. 7), suggest that other factors in addition to availability of dissolved iron controlled the production of magnetosomes during periods of rapidly changing palaeoenvironmental conditions. This illustrates complexities in the interplay between the supply of iron and magnetotactic bacterial productivity under changing climatic conditions (cf. Roberts et al., 2011). Regardless, this inferred causal link between aeolian dust and magnetosomes could provide an underlying explanation for the

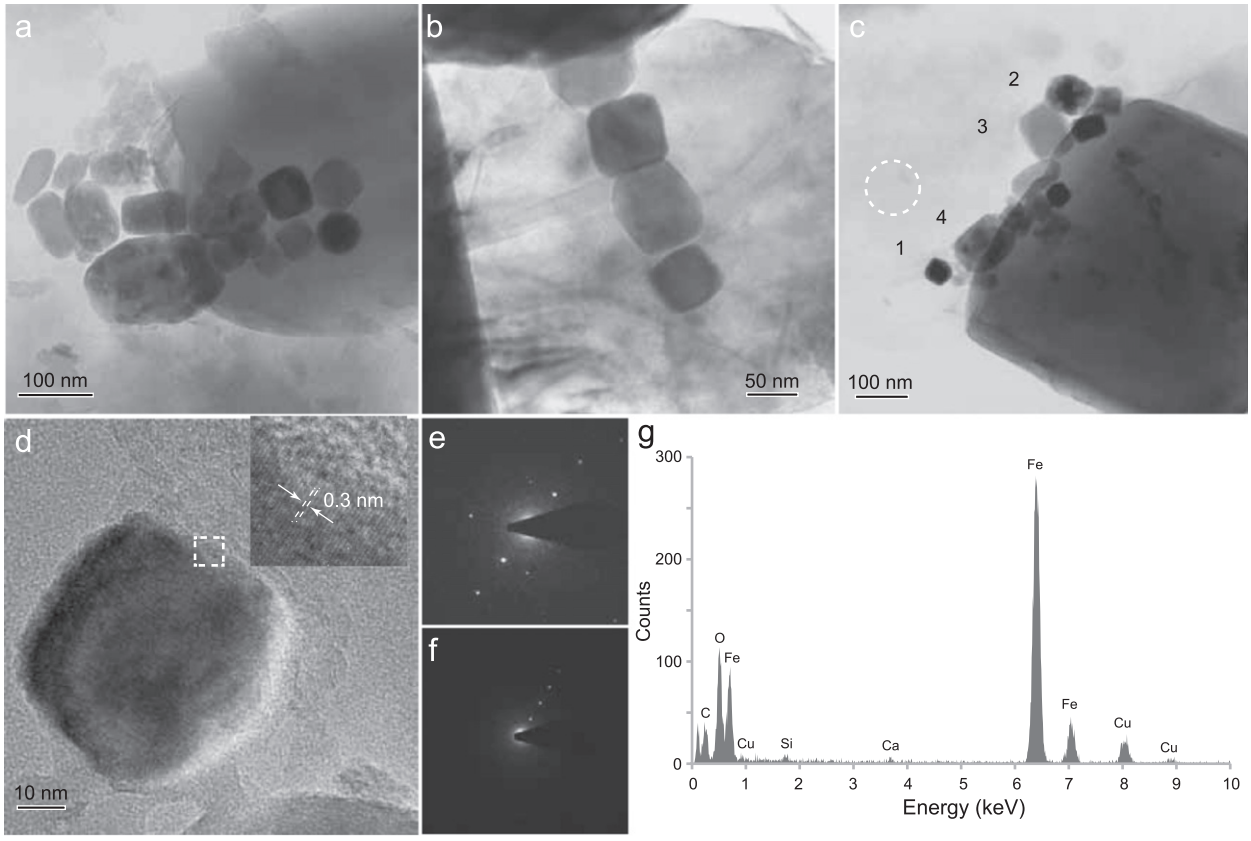

Fig. 6. Transmission electron microscope images and analyses of magnetic separates extracted from ODP Hole 738C sediments at 284.75 mbsf. (a, b, c) Groups and short chains of bacterial magnetofossils. The biogenic magnetite particles have a variety of typical magnetosome morphologies that include octahedra, elongated prisms and teardrops. (d) Lattice-resolution image of particle 1 in (c). The inset in the upper-right-hand side of (d) is a magnified view of the dashed box area that illustrates the clear lattice fringes at an interplanar spacing of 3.0 Å, that correspond to the {220} planes in magnetite. (e, f) Selected-area electron diffraction patterns for particles 1 and 2 in (c). The diffraction patterns with rows of reflections from lattice spacings of 3.0 Å and 4.8 Å, respectively, correspond to diffractions expected from magnetite {220} and {111} planes. (g) Energy-dispersive x-ray spectrum collected from particle 3 in (c). All analysed particles (1–4) in (c) gave rise to similar EDS spectra. The largest spectral peaks indicate that these nanoparticles consist of iron and oxygen and, together with the lattice spacings measured, demonstrate a magnetite composition. Cu peaks in the spectrum originate from the TEM grid. C is from the carbon film stretched across the TEM grid. The tiny Ca signal originates from the large calcium carbonate particle nearby (imaged on the right-hand side of (c)). The tiny Si peak arises from one of the many small, thin silicate particles scattered across the TEM grid; this was established by recording spectra from the area circled in (c) which is slightly darker than other areas of the bright background.

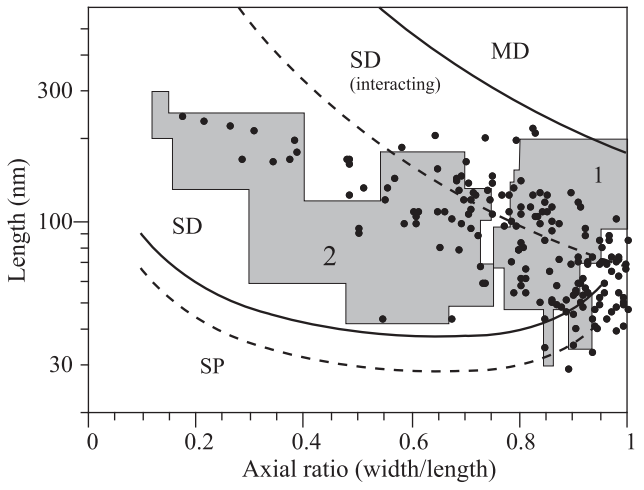

Fig. 7. Plot of length to axial ratio for magnetosomes from Hole 738C. The superparamagnetic (SP)/SD boundary is determined for crystals with unblocking times of 100 s (dashed line) and 4 Gy (solid line) according to Butler and Banerjee (1975). SD (interacting) indicates the field where magnetosomes behave as SD grains due to their interactions within the magnetosome chain (Muxworthy and Williams, 2006). The SD/MD boundary is after Muxworthy and Williams (2006). 1 and 2 denote the fields for magnetosomes with equidimensional and elongated shapes, respectively (Kopp and Kirschvink, 2008).

common, yet apparently overlooked, co-occurrence of aeolian dust and magnetofossils reported in deep-sea sediments from elsewhere in the world's oceans (e.g. Bloemendal et al., 1992; Yamazaki and Ioka, 1997; Dinarès-Turell et al., 2003; Yamazaki, 2009; Abrajevitch and Kodama, 2011). This mechanism would only be expected to be valid in oligotrophic open-ocean gyres in which iron is a limiting micronutrient and would not be expected to be valid in coastal settings or in marginal or restricted marine basins where primary production is not iron limited.

It appears that not only the concentration of magnetosomes, but also relative variations in their size, may be linked to climate variability throughout the PETM. Thus, ARM-CFB and χ_{ARM}/χ data indicate that decreased magnetosome concentrations at events c–e, when isotopically light carbon was being injected into the ocean–atmosphere system, was accompanied by a subtle (within the SD range) grain size coarsening (Fig. 8c, d). On the other hand, smaller magnetosome crystal sizes appear to be related to periods (event h) when organic carbon was being sequestered. The SD threshold size for magnetite is ten times larger for elongated than for equidimensional grains (e.g. for cubic SD grains it is <0.1 μm; for elongated SD grains it is <1 μm (e.g. Muxworthy and Williams, 2006; Kopp and Kirschvink, 2008)). It is therefore possible that changes in magnetosome grain size might be caused by variations in the relative concentration of elongated and equidimensional magnetosomes. These types of magnetosomes

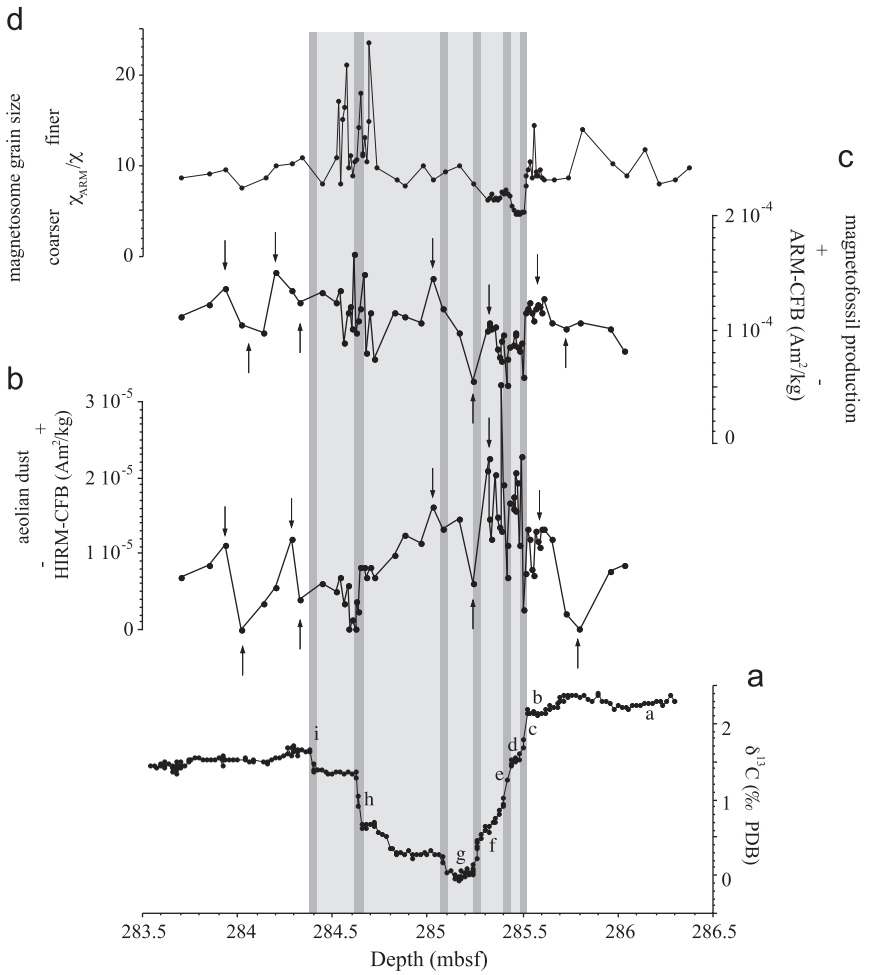

Fig. 8. Down-core variations in (a) bulk-sediment carbon isotopes, (b, c) ARM and HIRM calculated on a carbonate-free basis (CFB), and (d) magnetosome grain size across the PETM at ODP Hole 738C. Black arrows indicate the positions of peaks observed both in the ARM–CFB and HIRM–CFB curves.

are thought to be preferentially produced by magnetotactic bacteria under higher and lower organic carbon fluxes (e.g. Hesse, 1994; Yamazaki and Kawahata, 1998; Yamazaki, 2012). Potential changes in organic carbon contents associated with environmental variability during the PETM might have therefore conditioned such hypothesised changes in magnetosome morphology. However, other factors, such as the additional occurrence of giant magnetosomes of the type reported by Schumann et al. (2008), cannot currently be excluded for explaining the observed changes in magnetosome grain size (Chang et al., submitted). The Hole 738C PETM record presents a potentially useful case for future studies of changes in magnetofossil morphology in relation to $\delta^{13}C$ changes.

In order to improve our knowledge of links between magnetotactic bacterial activity and aeolian dust in response to climate variability during the PETM, we studied the rock magnetic properties of the PETM section recovered at ODP Hole 1051B (Fig. 1) (Bains et al., 1999), whose terrigenous sedimentation has been shown to be linked to changes in the supply of North African aeolian dust (Holmes et al., 2004). Our analyses of this deep-sea PETM section failed to identify magnetofossils despite evidence for the occurrence of magnetite and haematite of probable aeolian origin (see Appendix A). More detailed TEM and rock magnetic data will be necessary from Hole 738C and other PETM sections to establish any specific link between the abundance and grain size of magnetosomes and aeolian dust fluxes in response to climate variability during the PETM.

5. Conclusions

Bulk magnetic, hysteresis, FORC, FMR and TEM analyses of deep-sea sediments from Hole 738C, southern Kerguelen Plateau (Southern Ocean) demonstrate that biogenic magnetite is the dominant magnetic mineral not only during the PETM, as has been previously reported in shallower water sections (Lippert and Zachos, 2007; Kopp et al., 2007, 2009; Schumann et al., 2008), but also before and after the thermal event. This indicates that the occurrence of bacterial magnetosomes in the studied sediments is not due to a preservation effect linked to specific climatic or diagenetic conditions during or after the PETM, but that their concentration reflects sustained conditions that favoured continued magnetotactic bacterial activity. In addition to magnetofossils, the magnetic mineral assemblage of sediments from Hole 738C is characterised by the presence of aeolian haematite that is probably sourced from Antarctica. Aeolian haematite contents peaked at the beginning of the PETM and then progressively recovered back to pre-PETM values. This suggests increased aridity in Antarctica in response to rising global temperatures at the beginning of the PETM, which reinforces the idea that the interior of large continents experienced drier (at least seasonally) conditions at that time (Wing et al., 2005; Kraus and Riggins, 2007; Smith et al., 2009; Schulte et al., 2011; Sluijs et al., 2011; Handley et al., 2012) despite a globally enhanced hydrological cycle.

The coincidence between magnetosome concentrations and haematite abundances throughout most of the CIE suggests an

immediate response of magnetotactic bacterial activity to enhanced aeolian dust fluxes and hence to availability of dissolved iron. This indicates that iron fertilisation by aeolian dust during most of the PETM is likely to have been the main limiting factor that conditioned proliferation of magnetotactic bacteria in the deep sea, thereby reinforcing inferences by Roberts et al. (2011) based on the Eocene record from the southern Kerguelen Plateau. However, the striking decoupling between magnetosome abundances and aeolian dust fluxes at the onset and termination of the CIE suggests that other factors in addition to availability of dissolved iron controlled the production of magnetosmes during periods of rapidly changing palaeoenvironmental conditions. More detailed TEM and rock magnetic studies are needed for PETM sections worldwide to understand the details of palaeoenvironmental and diagenetic factors whose interactions contribute to production and preservation of magnetofossils in deep-sea sediments. Nevertheless, aeolian dust supply to iron-limited pelagic environments with expanded thicknesses of suboxic sediments appears to be fundamentally important for providing bioavailable iron to enhance magnetotactic bacterial populations.

Acknowledgements

Samples were provided by the IODP, which is sponsored by the U.S. National Science Foundation and participating countries under management of Joint Oceanographic Institutions, Inc. We are grateful to the staff from the IODP Core Repositories in Bremen and Kochi for technical assistance. We thank J. Wolowska for technical assistance with FMR measurements, which were made at the FMR National Service Centre at the University of Manchester, which is funded by the UK Engineering and Physical Sciences Research Council. We are also grateful for access to TEM equipment of the Centre for Advanced Microscopy in the ANU, which is a node of the Australian Microscopy and Microanalysis Research Facility. Shane Paxton provided valuable assistance with magnetic mineral separations. Liao Chang undertook the FMR measurements in conjunction with work funded by the NERC Grant NE/G003319/1 to Andrew Roberts. Stable isotope analytical work was supported by the NSF Grant EAR-0120727 to James Zachos. Andrew Roberts acknowledges a period of sabbatical leave from the University of Southampton that facilitated completion of aspects of this study. Juan C. Larrasoaña acknowledges the Spanish MEC (PR2011-0480) for funding a Visiting Fellowship at the ANU, where this study was completed. This work was started with financial support by the European Community TMR Network contract MAG-NET (ERBFMRXCT98-0247). We are also grateful to two anonymous reviewers whose constructive comments greatly improved the manuscript.

Appendix A. Supplementary materials

Supplementary data associated with this article can be found in the online version at http://dx.doi.org//10.1016/j.epsl.2012.04.003.

References

Abrajevitch, A., Kodama, K., 2009. Biochemical vs. detrital mechanism of remanence acquisition in marine carbonates: a lesson from the K–T boundary interval. Earth Planet. Sci. Lett. 286, 269–277.

Abrajevitch, A., Kodama, K., 2011. Diagenetic sensitivity of paleoenvironmental proxies: a rock magnetic study of Australian continental margin sediments. Geochem. Geophys. Geosyst. 12, Q05Z24, http://dx.doi.org/10.1029/2010GC003481.

Ali, J.R., Aitchison, J.C., 2009. Kerguelen Plateau and the Late Cretaceous southern-continent bioconnection hypothesis: tales from a topographical ocean. J. Biogeogr. 36, 1778–1784.

Arató, B., Szányi, Z., Flies, C., Schüler, D., Frankel, R.B., Buseck, P.R., Pósfai, M., 2005. Crystal-size and shape distributions of magnetite from uncultured magnetotactic bacteria as a potential biomarker. Am. Mineral. 90, 1233–1241.

Bains, S., Corfield, R.M., Norris, R.D., 1999. Mechanisms of climate warming at the end of the Paleocene. Science 285, 724–727.

Bains, S., Norris, R.D., Corfield, R.M., Faul, K.L., 2000. Termination of global warmth at the Palaeocene/Eocene boundary through productivity feedbacks. Nature 407, 171–174.

Banerjee, S.K., King, J., Marvin, J., 1981. A rapid method for magnetic granulometry with applications to environmental studies. Geophys. Res. Lett. 4, 333–336.

Bazylinski, D.A., Frankel, R.B., 2004. Magnetosome formation in prokaryotes. Nat. Rev. Microbiol. 2, 217–230.

Besse, J., Courtillot, V., 2002. Apparent and true polar wander and the geometry of the geomagnetic field over the last 200 Myr. J. Geophys. Res. 107 (B11), 2300, http://dx.doi.org/10.1029/2000JB000050.

Blain, S., et al., 2007. Effect of natural iron fertilization on carbon sequestration in the Southern Ocean. Nature 446, 1070–1074.

Bloemendal, J., King, J.W., Hall, F.R., Doh, S.J., 1992. Rock magnetism of Late Neogene and Pleistocene deep-sea sediments: relationships to sediment source, diagenetic processes, and sediment lithology. J. Geophys. Res. 97, 4361–4375.

Boughriet, A., Ouddane, B., Wartel, M., 1992. Electron spin resonance investigations of Mn compounds and free radicals in particles from the Seine River and its estuary. Mar. Chem. 37, 149–169.

Bowen, G.J., Beerling, D.J., Koch, P.L., Zachos, J.C., Quattlebaum, T., 2004. A humid climate state during the Palaeocene–Eocene thermal maximum. Nature 432, 495–499.

Butler, R.F., Banerjee, S.K., 1975. Theoretical single-domain grain size range in magnetite and titanomagnetite. J. Geophys. Res. 80, 4049–4058.

Chang, L., Roberts, A.P., Williams, W., Fitz Gerald, J.D., Larrasoaña, J.C., Jovane, L., Muxworthy, A.R., submitted for publication. Giant magnetofossils and hyperthermal events. Earth Planet. Sci. Lett.

Charilaou, M., Winklhofer, M., Gehring, A.U., 2011. Simulation of ferromagnetic resonance spectra of linear chains of magnetite nanocrystals. J. Appl. Phys. 109, 093903, http://dx.doi.org/10.1063/1.3581103.

Cramer, B.S., Kent, D.V., 2005. Bolide summer: the Paleocene/Eocene thermal maximum as a response to an extraterrestrial trigger. Palaeogeogr. Palaeoclimatol. Palaeoecol. 224, 144–166.

Day, R., Fuller, M., Schmidt, V.A., 1977. Hysteresis properties of titanomagnetites: grain size and composition dependence. Phys. Earth Planet. Inter. 13, 260–267.

Dickens, G.R., 1999. The blast in the past. Nature 401, 752–755.

Dickens, G.R., 2008. The riddle of the clays. Nat. Geosci. 1, 86–88.

Dinarès-Turell, J., Hoogakker, B.A.A., Roberts, A.P., Rohling, E.J., Sagnotti, L., 2003. Quaternary climatic control of biogenic magnetite production and eolian dust inputs in cores from the Mediterranean Sea. Palaeogeogr. Palaeoclimatol. Palaeoecol. 190, 195–209.

Dunlop, D.J., 2002. Theory and application of the Day plot (M_{rs}/M_s versus H_{cr}/H_c) 1. Theoretical curves and tests using titanomagnetite data. J. Geophys. Res. 107 (B3), 2056, http://dx.doi.org/10.1029/2001JB000486.

Egli, R., Chen, A.P., Winklhofer, M., Kodama, K.P., Horng, C.-S., 2010. Detection of noninteracting single domain particles using first-order reversal curve diagrams. Geochem. Geophys. Geosyst. 11, Q01Z11, http://dx.doi.org/10.1029/2009GC002916.

Ehrmann, W.U., 1991. Implications of sediment composition on the southern Kerguelen Plateau for paleoclimate and depositional environment. Proc. ODP Sci. Res. 119, 185–210.

Ehrmann, W.U., Mackensen, A., 1992. Sedimentological evidence for the formation of an East Antarctic ice sheet in Eocene/Oligocene time. Palaeogeogr. Palaeoclimatol. Palaeoecol. 93, 85–112.

Evans, M.E., Heller, F., 2003. Environmental Magnetism. Principles and Applications of Enviromagnetics. Academic Press (pp. 299).

Faivre, D., Schüler, D., 2008. Magnetotactic bacteria and magnetosomes. Chem. Rev. 108, 4875–4898.

Fischer, H., Mastrogiacomo, G., Löffler, J.F., Warthmann, R.J., Weidler, P.G., Gehring, A.U., 2008. Ferromagnetic resonance and magnetic characteristics of intact magnetosome chains in *Magnetospirillum gryphiswaldense*. Earth Planet. Sci. Lett. 270, 200–208.

Frank, U., Nowaczyk, N.R., 2008. Mineral magnetic properties of artificial samples systematically mixed from haematite and magnetite. Geophys. J. Int. 175, 449–461.

Frey, F.A., et al., 2000. Origin and evolution of a submarine large igneous province: the Kerguelen Plateau and Broken Ridge, southern Indian Ocean. Earth Planet. Sci. Lett. 176, 73–89.

Gehring, A.U., Kind, J., Charilaou, M., García-Rubio, I., 2011. The detection of magnetotactic bacteria and magnetofossils by means of magnetic anisotropy. Earth Planet. Sci. Lett. 309, 113–117.

Handley, L., O'Halloran, A., Pearson, P.N., Hawkins, E., Nicholas, C.J., Schouten, S., McMillan, I.K., Pancost, R.D., 2012. Changes in the hydrological cycle in tropical East Africa during the Paleocene–Eocene thermal maximum. Palaeogeogrphy Palaeoclimatology Palaeoecology, 329–330, 10–21.

Hesse, P.P., 1994. Evidence for bacterial palaeoecological origin of mineral magnetic cycles in oxic and sub-oxic Tasman Sea sediments. Mar. Geol. 117, 1–17.

Holmes, M.A., Watkins, D.K., Norris, R.D., 2004. Paleocene cyclic sedimentation in the western North Atlantic, ODP site 1051 Blake Nose. Mar. Geol. 209, 31–43.

Kelly, D.C., Zachos, J.C., Bralower, T.J., Schellenberg, S.A., 2005. Enhanced terrestrial weathering/runoff and surface ocean carbonate production during the recovery stages of the Paleocene–Eocene thermal maximum. Paleoceanography 20, PA4023, http://dx.doi.org/10.1029/2005PA001163.

Kent, D.V., Cramer, B.S., Lanci, L., Wang, D., Wright, J.D., Van der Voo, R., 2003. A case for a comet impact trigger for the Paleocene/Eocene thermal maximum and carbon isotope excursion. Earth Planet. Sci. Lett. 211, 13–26.

King, J., Banerjee, S.K., Marvin, J., Özdemir, Ö., 1982. A comparison of different magnetic methods for determining the relative grain size of magnetite in natural materials—some results from lake sediments. Earth Planet. Sci. Lett. 59, 404–419.

Kopp, R.E., Kirschvink, J.L., 2008. The identification and biogeochemical interpretation of fossil magnetotactic bacteria. Earth Sci. Rev. 86, 42–61.

Kopp, R.E., Weiss, B.P., Maloof, A.C., Vali, H., Nash, C.Z., Kirschvink, J.L., 2006. Chains, clumps, and strings: magnetofossil taphonomy with ferromagnetic resonance spectroscopy. Earth Planet. Sci. Lett. 247, 10–25.

Kopp, R.E., Raub, T.D., Schumann, D., Vali, H., Smirnov, A.V., Kirschvink, J.L., 2007. Magnetofossil spike during the Paleocene–Eocene thermal maximum: ferromagnetic resonance, rock magnetic, and electron microscopy evidence from Ancora, New Jersey, United States. Paleoceanography 22, PA4103, http://dx.doi.org/10.1029/2007PA001473.

Kopp, R.E., Schumann, D., Raub, T.D., Powars, D.S., Godfrey, L.V., Swanson-Hysell, N.L., Maloof, A.C., Vali, H., 2009. An Appalachian Amazon? Magnetofossil evidence for the development of a tropical river-like system in the mid-Atlantic United States during the Paleocene–Eocene Thermal Maximum. Paleoceanography 24, PA4211, http://dx.doi.org/10.1029/2009PA001783.

Kraus, M.J., Riggins, S., 2007. Transient drying during the Paleocene–Eocene Thermal Maximum (PETM): analysis of paleosols in the Bighorn Basin Wyoming. Palaeogeogr. Palaeoclimatol. Palaeoecol. 245, 444–461.

Lean, C.M.B., McCave, I.N., 1998. Glacial to interglacial mineral magnetic and palaeoceanographic changes at Chatham Rise, SW Pacific Ocean. Earth Planet. Sci. Lett. 163, 247–260.

Lippert, P.C., Zachos, J.C., 2007. A biogenic origin for anomalous fine-grained magnetic material at the Paleocene–Eocene boundary at Wilson Lake, New Jersey. Paleoceanography 22, PA4104, http://dx.doi.org/10.1029/2007PA001471.

Maher, B.A., Prospero, J.M., Mackie, D., Gaiero, D., Hesse, P.P., Balkanski, Y., 2010. Global connections between aeolian dust, climate and ocean biogeochemistry at the present day and at the last glacial maximum. Earth Sci. Rev. 99, 61–97.

Muxworthy, A.R., Williams, W., 2006. Critical single-domain/multi-domain grain sizes in noninteracting and interacting elongated magnetite particles: implications for magnetosomes. J. Geophys. Res. 111, B12S12, http://dx.doi.org/10.1029/2006JB004588.

Otamendi, A.M., Díaz, M., Costanzo-Álvarez, V., Aldana, M., Pilloud, A., 2006. EPR stratigraphy applied to the study of two marine sedimentary sections in southwestern Venezuela. Phys. Earth Planet. Inter. 154, 243–254.

Peters, C., Dekkers, M.J., 2003. Selected room temperature magnetic parameters as a function of mineralogy, concentration and grain size. Phys. Chem. Earth 28, 659–667.

Pollard, R.T., et al., 2007. Southern Ocean deep-water carbon export enhanced by natural iron fertilization. Nature 457, 577–580.

Poulton, S.W., Krom, M.D., Raiswell, R., 2004. A revised scheme for the reactivity of iron (oxyhydr)oxide minerals towards dissolved sulfide. Geochim. Cosmochim. Acta 68, 3703–3715.

Roberts, A.P., Pike, C.R., Verosub, K.L., 2000. First-order reversal curve diagrams: a new tool for characterizing the magnetic properties of natural samples. J. Geophys. Res. 105, 28461–28475.

Roberts, A.P., Florindo, F., Villa, G., Chang, L., Jovane, L., Bohaty, S.M., Larrasoaña, J.C., Heslop, D., Fitz Gerald, J.D., 2011. Magnetotactic bacterial abundance in pelagic marine environments is limited by organic carbon flux and availability of dissolved iron. Earth Planet. Sci. Lett. 310, 441–452.

Schmitz, B., Pujalte, V., 2007. Abrupt increase in seasonal extreme precipitation at the Paleocene–Eocene boundary. Geology 35, 215–218.

Schulte, P., Scheibner, C., Speijer, R.P., 2011. Fluvial discharge and sea-level changes controlling black shale deposition during the Paleocene–Eocene Thermal Maximum in the Dababiya Quarry section, Egypt. Chem. Geol. 285, 167–183.

Schumann, D., Raub, T.D., Kopp, R.E., Guerquin-Kerne, J.L., Wue, T.D., Rouiller, I., Smirnov, A.V., Kelly Sears, S., Lücken, U., Tikoo, S.M., Hesse, R., Kirschvink, J.L., Vali, H., 2008. Gigantism in unique biogenic magnetite at the Paleocene–Eocene Thermal Maximum. Proc. Natl. Acad. Sci. USA 105, 17648–17653.

Shipboard Scientific Party, 1989. Site 738. Proceedings of the Ocean Drilling Program, Initial Reports, vol. 119, pp. 229–288.

Sluijs, A., Bijl, P.K., Röhl, U., Reichart, G.J., Brinkhuis, H., 2011. Southern ocean warming, sea level and hydrological change during the Paleocene–Eocene Thermal Maximum. Clim. Past 7, 47–61.

Smith, J.J., Hasiotis, S.T., Kraus, M.J., Woody, D.T., 2009. Transient dwarfism of soil fauna during the Paleocene–Eocene Thermal Maximum. Proc. Natl. Acad. Sci. USA 106, 17655–17660.

Stanley, S.M., 2010. Relation of Phanerozoic stable isotope excursions to climate, bacterial metabolism, and major extinctions. Proc. Natl. Acad. Sci. USA 107, 19185–19189.

Stolz, J.F., Chang, S.B.R., Kirschvink, J.L., 1986. Magnetotactic bacteria and single-domain magnetite in hemipelagic sediments. Nature 321, 849–851.

Tarduno, J.A., Wilkison, T.W., 1996. Non-steady state magnetic mineral reduction, chemical lock-in, and delayed remanence acquisition in pelagic sediments. Earth Planet. Sci. Lett. 144, 315–326.

Weiss, B.P., Kim, S.S., Kirschvink, J.L., Kopp, R.E., Sankaran, M., Kobayashi, A., Komeili, A., 2004. Ferromagnetic resonance and low temperature magnetic tests for biogenic magnetite. Earth Planet. Sci. Lett. 233, 311–324.

Wing, S.L., Harrington, G.J., Smith, F.A., Bloch, J.I., Boyer, D.M., Freeman, K.H., 2005. Transient floral change and rapid global warming at the Paleocene–Eocene boundary. Science 310, 993–996.

Woodard, S.C., Thomas, D.J., Hovan, S., Röhl, U., Westerhold, T., 2011. Evidence for orbital forcing of dust accumulation during the early Paleogene greenhouse. Geochem. Geophys. Geosyst. 12, Q02007, http://dx.doi.org/10.1029/2010GC003394.

Yamazaki, T., 2009. Environmental magnetism of Pleistocene sediments in the North Pacific and Ontong-Java Plateau: temporal variation of detrital and biogenic components. Geochem. Geophys. Geosyst. 10 http://dx.doi.org/10.1029/2009GC002413Q07Z04 http://dx.doi.org/10.1029/2009GC002413.

Yamazaki, T., 2012. Paleoposition of Intertropical Convergence Zone in the eastern Pacific inferred from glacial–interglacial changes in terrigenous and biogenic magnetic mineral fractions. Geology 40, 151–154.

Yamazaki, T., Ioka, N., 1997. Environmental rock-magnetism of pelagic clay: implications for Asian eolian input to the North Pacific since the Pliocene. Paleoceanography 12, 111–124.

Yamazaki, T., Kawahata, H., 1998. Organic carbon flux controls the morphology of magnetofossils in marine sediments. Geology 26, 1064–1066.

Zachos, J.C., Röhl, U., Schellenberg, S.A., Sluijs, A., Hodell, D.A., Kelly, D.C., Thomas, E., Nicolo, M., Raffi, I., Lourens, L.J., McCarren, H., Kroon, D., 2005. Rapid acidification of the ocean during the Paleocene–Eocene Thermal Maximum. Science 308, 1611–1615.